RESEARCH ARTICLE | AUGUST 23 2023

Evolution of high-density submarine turbidity current and its interaction with a pair of parallel suspended pipes

Special Collection: Recent Advances in Marine Hydrodynamics

Xingsen Guo (郭兴森) ; Qianyu Luo (罗倩钰) ; Thorsten Stoesser ; Arthur Hajaali ; Xiaolei Liu (刘晓磊)

Physics of Fluids 35, 086608 (2023)
https://doi.org/10.1063/5.0160650

Physics of Fluids ARTICLE pubs.aip.org/aip/pof

Evolution of high-density submarine turbidity current and its interaction with a pair of parallel suspended pipes

Cite as: Phys. Fluids **35**, 086608 (2023); doi: 10.1063/5.0160650
Submitted: 4 June 2023 · Accepted: 3 August 2023 ·
Published Online: 23 August 2023

Xingsen Guo (郭兴森),[1,2,3,4,a)] Qianyu Luo (罗倩钰),[2,a)] Thorsten Stoesser,[2,b)] Arthur Hajaali,[2,a)] and Xiaolei Liu (刘晓磊)[1,5,b)]

AFFILIATIONS

[1]Shandong Provincial Key Laboratory of Marine Environment and Geological Engineering, Ocean University of China, Qingdao 266100, China
[2]Department of Civil, Environmental and Geomatic Engineering, University College London, London WC1E 6BT, United Kingdom
[3]State Key Laboratory of Coastal and Offshore Engineering, Dalian University of Technology, Dalian 116024, China
[4]State Key Laboratory of Geohazard Prevention and Geoenvironment Protection, Chengdu University of Technology, Chengdu 610059, China
[5]Laboratory for Marine Geology, Qingdao National Laboratory for Marine Science and Technology, Qingdao 266061, China

Note: This paper is part of the special topic, Recent Advances in Marine Hydrodynamics.
[a)]**Electronic addresses**: xingsen.guo@ucl.ac.uk; qianyu.luo.18@ucl.ac.uk; and a.hajaali@ucl.ac.uk
[b)]**Authors to whom correspondence should be addressed:** t.stoesser@ucl.ac.uk and xiaolei@ouc.edu.cn

ABSTRACT

The method of large-eddy simulation (LES) coupled with the density transport equation is employed to simulate the evolution of a gravity-driven high-density turbidity current and its interaction with a pair of parallel suspended pipes. The LES method is validated first using data of a non-Boussinesq lock-exchange experiment and satisfying agreement between LES and experiment is achieved. The simulations reveal that a shear region forms between high- and low-density fluids each moving in opposite directions which lead to the generation of a series of vortices and a substantial mixing region. Close to the bottom boundary, low-density fluid is entrained near the head of the high-density turbidity current, forming a thin water cushion that separates the turbidity current's head from the seabed, the so-called hydroplaning effect, thereby reducing the density of the head and bottom friction. The current study suggests that the effect of hydroplaning phenomena leads to high speed and long distance of the turbidity current. Further, LES simulations of a turbidity current impacting a pair of parallel suspended pipes with different streamwise spacings are performed and impact forces are quantified. The turbulent wake generated by high-density fluid bypassing pipe 1 promotes velocity fluctuations leading to increased impact forces on pipe 2 with increasing streamwise spacing up to 8 times the pipeline diameter ($8D$). The results suggest that the streamwise spacing between two parallel pipes should be less than $2D$ to minimize hydrodynamic loads on pipe 2.

I. INTRODUCTION

A submarine turbidity current is a gravity-induced geological phenomenon and also constitutes an important stage of a submarine slide (e.g., density flow, gravity flow, and suspended particle flow).[1–3] It is the most significant geological process for transport of sediments over long distances.[2,4–8] A large amount of sediments, millions of cubic meters, can be transported by a turbidity current to deep-sea basins reaching hundreds or even thousands of kilometers over short periods of time, reflecting that turbidity currents are characterized by high velocity, strong transport capacity, and long run-out distances.[9–14] For instance, the amount of sediments transported by a large turbidity current even exceeds the total amount of sediments discharged into seas by all rivers in a year.[15] Due to the enormous transport capacity, turbidity currents bring a large amount of land-source nutritional salts and form turbidity fans that are highly susceptible to impact reservoirs of hydrocarbon resources.[16–18] Turbidity currents also bring a lot of microplastics that pollute the marine ecological environment.[19] The high concentration of suspended sediments within turbidity currents

supported by turbulence[12,20–23] exhibits strong destructive capacity and poses a huge threat to engineering facilities, such as pipelines.[20,24–26] Thus, studies on the migration and evolution of turbidity currents are the key not only to solve basic scientific problems related to marine geology, hydrodynamics, and sedimentation but also to guide marine ecological protection, mineral resources development, and engineering disaster prevention.[1,2,6,27]

Extensive research has been conducted on the complex phenomena of submarine turbidity currents, which can be categorized by the scale at which the research was undertaken. *In situ* observations and geological surveys are devoted to monitoring and inversion of events of large-scale turbidity currents.[18,28–32] However, such monitoring still faces challenges due to the unpredictability of turbidity currents. Laboratory-scale experiments and numerical simulations are mostly performed to reproduce the movement process of turbidity currents and reveal physical mechanisms governing run-out distance, hydrodynamics, and mass transport. Hampton[33] conducted laboratory-scale flume experiments and found that the evolution phenomenon of gravity flow is mainly governed by processes taking place in its head and top and pointed out ambient water is entrained along the current top's turbulent area. Hotta *et al.*[34] implemented centrifugal model experiments to demonstrate the hydroplaning effect of gravity flows, supporting the mechanism of high velocity and long distance, and reproducing the density reduction phenomenon of gravity currents. However, these physical flume experiments used a mixture of clay and water to simulate submarine turbidity currents, and the rapid mixing resulted in missing data, lack of clarity, and suffers difficulty in capturing the evolution of flow fields,[20,35–37] which is difficult to explain in detail the triggering mechanisms of these phenomena. Keulegan[38] proved that turbidity currents could be simulated by saltwater density flows, providing a convenient visualization of flow fields.[39] These physical model experiments effectively supported the development of subsequent numerical methods.[38–40]

Numerical simulation is a highly effective method to investigate the evolution of turbidity currents and corresponding mechanisms.[41–44] Common numerical methods involve computational fluid dynamics (CFD),[6,39,45–54] smooth particle hydrodynamics (SPH),[55,56] material point method (MPM),[57,58] moving particle semi-implicit method (MPS),[59,60] CFD-DEM (discrete element method) coupling method,[61–63] and CFD-MPM coupling method.[64] Here, particle methods have a natural advantage in probing the behavior of particulate matter during the movement of sandy turbidity currents. Nevertheless, the simulation of the actual particle size is very expensive and difficult to achieve. CFD methods are more suitable for submarine turbidity currents with a large proportion of clay sediment and have great advantages in accurately resolving the evolution of flow fields.[65] Without considering the mass transport of turbidity current and ambient water, CFD methods are widely used to study the instantaneous motion of submarine turbidity currents at flume scale, well reproducing the head velocity[26] and impact forces on pipes.[25,52,66] However, focusing on the evolutionary processes of high-density submarine turbidity currents, mass transport must be considered.[50,54] Turbulent mixing caused by the propagation of turbidity current is an important topic;[67] however, few studies quantified the mixing effect of a turbidity current with ambient water and the underlying support mechanisms.[27] For the kinematic evolution of low-density turbidity currents (i.e., the density difference between turbidity currents and ambient water is very small), many researchers simulated the evolution of concentration using the scalar transport equation.[39,43,68–73] Significantly, the evolutionary process of the density field in the interaction between low-density turbidity currents and ambient water and the contribution of density variation to overall flow fields are neglected. In many engineering cases, the density difference between turbidity current and ambient water is very large, and the large density difference not only is the driving force but also plays a decisive role in the evolution of turbidity currents and disaster assessments, which needs to be further explored.[74] Submarine turbidity currents have caused damage to many offshore pipelines.[24,36,75] In past studies, many CFD simulations have focused on the impact of submarine landslides on a single pipeline;[25,52,66,76–79] however, these studies have neglected the evolution/change in fluid density during the movement of submarine landslides. Furthermore, the impact of high-density submarine turbidity currents on more complex structures (i.e., suspended pipelines without seabed protection are more prone to vortex-induced vibration compared to buried and laid-on-seafloor pipelines), taking into account the change in fluid density and the pipelines' spacing, requires further studies. This paper addresses the knowledge gap by investigating the hydrodynamics of a turbidity current and its interaction with a pair of submerged pipes via large-eddy simulations (LES). The objectives are to quantify the hydrodynamic loading on both the upstream and downstream situated pipe and to demonstrate the effect of pipe spacing on these loads.

The remainder of this paper is organized as follows. In Sec. II, the numerical framework for simulating the density evolution of a high-density turbidity current in ambient water through the incompressible continuity, Navier–Stokes, and density transport equations is introduced, and computational setups of large-eddy simulation cases are presented. In Sec. III, Lowe *et al.*[80] lock-exchange experiment of a non-Boussinesq case is used to validate the numerical method, involving the distribution of mixing densities, and head velocities of the high and low-density fluids; then, the turbulent mixing process of high- and low-density fluids is revealed, followed by a discussion of the development of turbulent mixing and bottom intrusion, providing new insights to demonstrate their potential for creating damage; and finally, loads of a high-density turbidity current on a pair of parallel suspended pipes with varying streamwise spacings are quantified and discussed. The conclusions are presented in Sec. IV.

II. METHODOLOGY

A. Numerical framework

The open-source large-eddy simulation code Hydro3D is employed to simulate the evolution of high-density turbidity current and its interaction with a pair of parallel suspended pipes with different streamwise spacings. The code has been validated successfully for and applied to a number of similar environmental and engineering flows,[81,82] such as the transport of a passive scalar in a turbulent flow,[83] transport and deposition of fine sediment in open channels,[84] and enhanced mixing with buoyant plumes.[85] In this study, the Boussinesq approximation is used to account for stratification effects, where the effect of density is only accounted for in the gravitational term. The code solves the spatially filtered Navier–Stokes equations in an Eulerian framework reading

$$\nabla \cdot \mathbf{u} = 0, \tag{1}$$

$$\frac{\partial \mathbf{u}}{\partial t} = -\frac{1}{\rho_0}\nabla p - \mathbf{u}\cdot\nabla\mathbf{u} + \nu\nabla^2\mathbf{u} - \nabla\tau_{SGS} + \frac{\rho \boldsymbol{g}}{\rho_0} + \mathbf{f}, \tag{2}$$

where $\mathbf{u}$ denotes the filtered resolved velocity field, p denotes the pressure, ν is the kinematic viscosity, $\mathbf{f}$ represents the volume force of the immersed boundary method (representing the pipes) exerted to the fluid, and $\mathbf{g}$ is the gravitational acceleration. The sub-grid scale stress tensor, τ_{SGS}, results from unresolved small-scale fluctuations and is approximated by the wall-adapting local eddy-viscosity (WALE) model[86] for all the cases presented in this paper. Hydro3D is based on finite differences with staggered storage of three-dimensional velocity components and central storage of pressure on Cartesian grids. The governing equations (1) and (2) are advanced in time by the fractional-step method.[87] In the predictor step, convection and diffusion terms are solved via an explicit three-step Runge–Kutta predictor. Fourth- and second-order central differences schemes are used to approximate convective and diffusive terms, respectively. In the corrector step, the pressure and a divergence-free velocity field are obtained by solving the Poisson equation via a multigrid iteration scheme.[88]

The transport of the density is simulated in an Eulerian framework by solving a filtered convection–diffusion equation. The filtered transport equation is solved at each time step once the fluid field is calculated, which reads

$$\frac{\partial \rho}{\partial t} = K\nabla^2\rho - \nabla\cdot(\mathbf{u}\rho), \tag{3}$$

where $K = \nu/Sc$ is the diffusion coefficient, depending on the Schmidt number Sc and kinematic viscosity ν. The updated density field is then taken into account in the Navier–Stokes equations, i.e., Eqs. (1) and (2), in the next time step. The convective term in the transport equation (3) is discretized using the second-order upwind differencing scheme.

Spatial-decomposition-based standard message passing interface (MPI) is used to accomplish the communications between pre-allocated computational subdomains, which is necessary to manage the computational load to provide sufficiently fine grids in LES.[89]

B. Computational setups

This study assumes that high-density turbidity current (i.e., gravity flow) is a homogeneous Newtonian fluid. The setup of the simulation of a high-density turbidity current is selected in analogy to the laboratory experiment undertaken by Lowe *et al.*[80] The experiment was performed in a closed rectangular channel, and a sodium iodide solution (NaI) was chosen as the heavier fluid while fresh comprised the lighter fluid. The dimensions (i.e., $x_0 = 1.83$ m, $y_0 = 0.23$ m, and $z_0 = 0.2$ m) of the channel are depicted in Fig. 1. The lock gate was placed in the middle of the channel and was removed rapidly along the vertical direction to initiate the non-Boussinesq lock-exchange experiment.

The computational domain of the lock-exchange simulation corresponds exactly to the experimental flume by Lowe *et al.*,[80] and the resulting flow features Reynolds and Froude numbers 95, 500, or 0.378, respectively. These are based on the head velocity of the heavier current 0.4775 m/s and the reference height 0.2 m. The no-slip condition is applied at all boundaries of the channel to mimic the Plexiglas sheets used in the experiment. The kinematic viscosity $\nu = 0.01\ \mathrm{cm^2/s}$ of both fluids is kept to be constant[42] during the simulation which results in a varying dynamic viscosity with density. The computational domain is discretized using a uniform grid in the streamwise (x), spanwise (y), and wall-normal (z) directions. Throughout this paper, the velocity components in the streamwise (x), spanwise (y), and wall-normal (z) directions are denoted as u, v, and w, respectively.

Upon successful validation, a series of LES consisting of 15 runs are further performed with the goal to investigate the impact of the turbidity current on a pair of parallel suspended pipes with varying streamwise spacing. The pipes are represented by the immersed boundary method for fast and efficient execution of the solver despite the complexity of the flow domain. The validity of the immersed boundary method and the assessment of its impact forces on structures in the current code were established previously for various complex flows such as flow over square bars,[90,91] the impact of environmental turbulence on the performance and loadings of a tidal stream turbine,[92] and flow through the bridge abutment openings.[93]

III. RESULTS AND DISCUSSION

A. Validation

In the first step, the LES code is validated using data of the lock-exchange experiment by Lowe *et al.*,[80] to confirm the adequacy of the selected discretization schemes, the grid size, subgrid-scale model, and boundary conditions, respectively. Table I presents four LES validation cases ($Sc = 0.1$). The LES-computed position of each of the two fluids' head as a function of time is shown in Fig. 2 demonstrating convincing quantitative agreement with the measured data. There is a shift in the data of the simulation compared to the lock-exchange experiment, which is most likely due to the initialization of the experiment, i.e., a physical gate is being pulled up in the experiment which introduces some additional momentum to the flow, while there is no gate in the

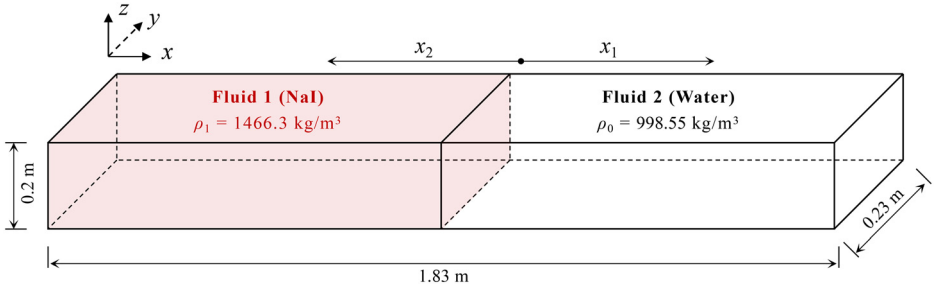

FIG. 1. Sketch of experimental setup and computational domain.

TABLE I. Grid resolution of the four LES validation cases.

Run	Grid resolution (m)	Time step
A	0.005	Variable
B	0.0025	Variable
C	0.00125	Variable
D	0.0025	Fixed

simulation. Specifically, in the physical experiment it takes a little bit of time to pull away the gate, which causes the head of the high-density fluid to run out first (or get a headstart), which is the reason why there is a constant shift to the simulation's head location. Apart from this shift, over the entire experiment, the calculated slope of both lines shown in Fig. 2 is in very good agreement with the experimental data (black crosses). The grid of $7320 \times 92 \times 80 (= 5.4 \times 10^7)$ points (case B) in x, y, and z directions, respectively, is sufficiently fine as seen from a grid sensitivity analysis, only the results on the coarsest grid are not as accurate. Take case B as an example, this case uses 61 cores to compute 6000 time steps (real time is 2.06 s), and the entire computation takes 11 377 s.

With a focus on the mixing process of the two fluids with a large density difference, the subgrid-scale scalar diffusion coefficient K may influence the results of the simulation, especially when the grid is coarse. The effect of the diffusion coefficient, i.e., the ratio between kinematic viscosity ν and Schmidt number Sc is investigated, and because the kinematic viscosity of the two fluids is equal ($\nu = 1 \times 10^{-6} \mathrm{m}^2/\mathrm{s}$), the diffusion coefficient K depends only on Sc. Figure 3 plots the head position of the two fluids as a function of time

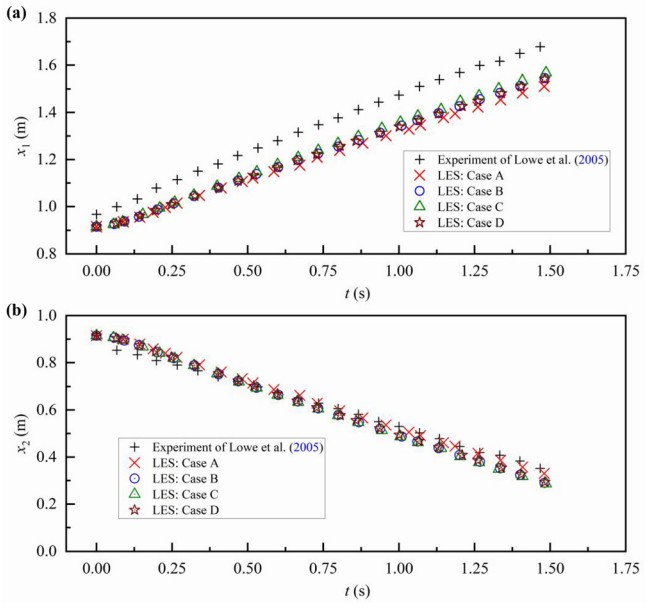

FIG. 2. Position of the head of the two fluids as functions of time ($Sc = 0.1$): (a) high-density fluid (NaI) and (b) low-density fluid (water).

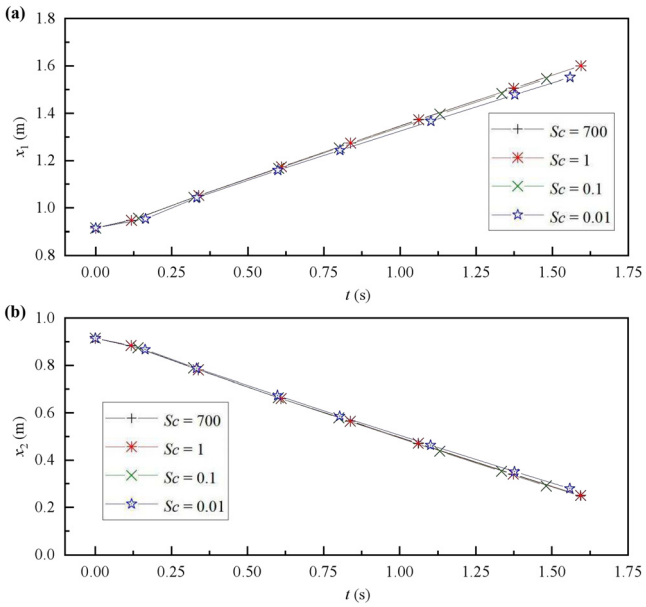

FIG. 3. The head position of two fluids as functions of time using different Schmidt numbers: (a) high-density fluid (NaI) and (b) low-density fluid (water).

for different Schmidt numbers (i.e., $Sc = 0.01$, $Sc = 0.1$, $Sc = 1$, and $Sc = 700$) and Fig. 4 presents sequential views visualizing fluid motions and mixing for different Schmidt numbers. The results show that Sc barely affects the head velocity of the low/high-density fluids, while it affects somewhat the mixing process. Some differences regarding the interface between the two fluids across varying Sc are observed when $t > 0.33$s. When Sc is very small, e.g., $Sc = 0.01$, the mixing effect is enhanced, most notably when comparing simulation (a) with (d) for the last time step plotted. Especially in Reynolds-Averaged-Navier-Stokes-based simulations, Sc has a much bigger effect and ranges between 0.1 and 700;[94] in LES, the sub-grid diffusion coefficient is deemed insignificant due to the large-scale and most energetic turbulence being resolved by the grid as demonstrated in Fig. 5.

Figure 5 presents sequential views of the two fluids visualizing the evolution of the gravity current over time. The simulation appears to be reproducing well the interface between the gravity current and the lighter fluid and the mixing of the two fluids due to local shear-generated turbulence in the form of Kelvin–Helmholtz instabilities[95] along the top of the heavier fluid and close to the front. The simulation also features the intrusion of low-density fluid near the front along the bed forming a light-fluid cushion below the head of the high-density fluid, the so-called hydroplaning effect, which is consistent with the experimental observation by Lowe *et al.*[80] This phenomenon reduces the friction between the high-density fluid and the bottom boundary, which is an important internal mechanism that leads to the high-velocity, long-distance, and long-time transport of submarine turbidity currents on the seabed.[96,97] In summary, the numerical framework presented in Sec. II is capable of reproducing accurately the flow and mixing of two fluids with large density differences to support the subsequent numerical analysis.

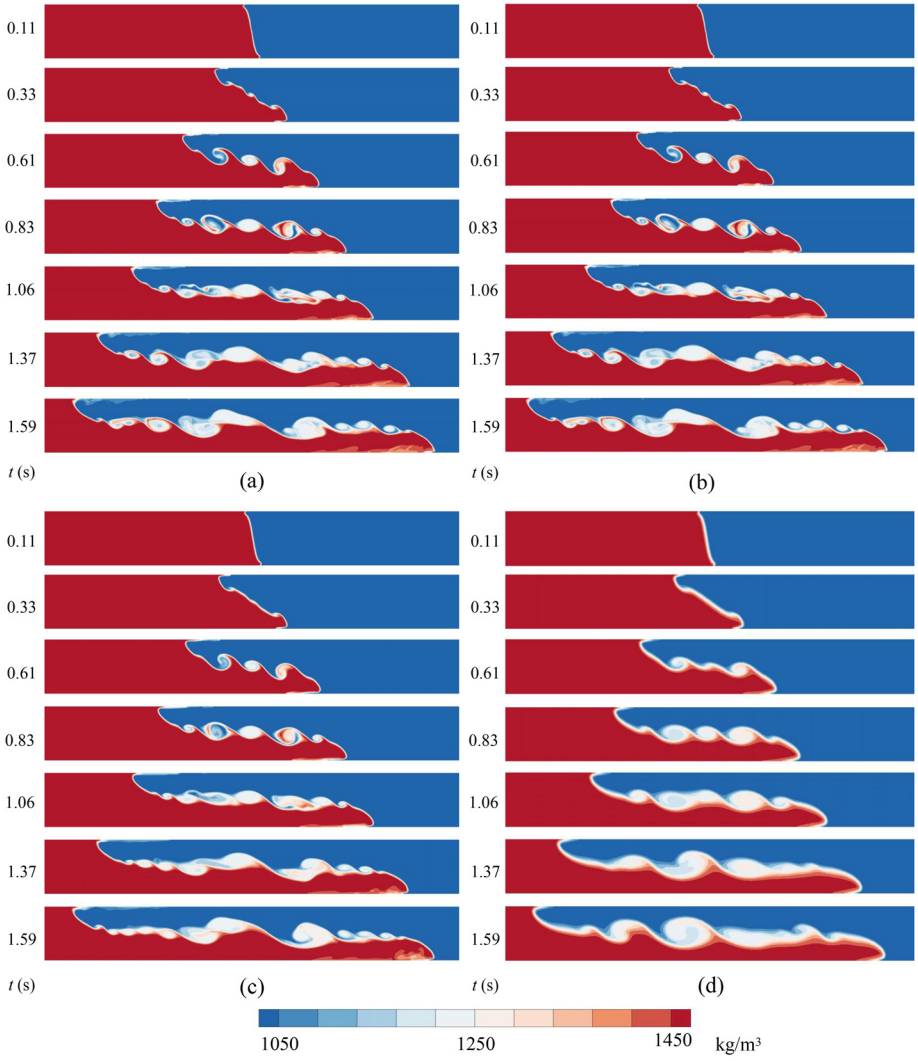

FIG. 4. Sequential view of the two fluid motions accompanying their mixing process at different Schmidt number conditions: (a) $Sc = 700$, (b) $Sc = 1$, (c) $Sc = 0.1$, and (d) $Sc = 0.01$.

B. Hydrodynamics of a high-density turbidity current in ambient water

Figure 6 presents contours of the streamwise and vertical velocity for various instants in time. The highest streamwise velocity occurs at the waist of the high-density fluid due to the collapse of the high-density fluid under the action of gravity and drives the movement of the high-density fluid head. High- and low-density fluids have opposite directions of motion, which generates a strong shear layer and, hence, a large number of vortices along the interface, seen in the changing of sign in the vertical velocity (when $t > 0.67$ s). As the gravity current progresses in time its velocity remains constantly high and vortices persist along the entire interface. Figure 7 presents contours of the density gradient of the two fluids in the streamwise (a) and vertical (b) directions at different instants in time. The two fluids are mixed efficiently in the shear layer or interface, respectively, and the mixing region gradually expands in the streamwise directions with increasing migration time. The shear-layer vortices (or Kelvin–Helmholtz billows) are characterized by alternating negative and positive streamwise gradients. The hydroplaning is characterized by significant positive vertical gradients of the density which accelerates the gravity current near the bed and decelerates the lighter-fluid current near the top of the domain.

Figure 8 presents the components of energy per unit length in the y direction as a function of time. The two fluids in the computational domain are static initially and only (gravitational) potential energy prevails. Driven by gravity, the high- and low-density fluids start to move, and potential energy is converted into kinetic energy, while some energy is dissipated mainly due to friction. The total energy at any instant in time is equal to the sum of kinetic energy (kinetic energy of each unit: KE/dy, where $KE = 0.5\rho \cdot dx \cdot dy \cdot dz \cdot (u^2 + w^2)$, while v is negligibly small) and potential energy (gravitational potential energy of each unit: GE/dy, where $GE = \rho \cdot dx \cdot dy \cdot dz \cdot g \cdot z$, and z at the bottom boundary is 0). Energy dissipation includes the following two processes: (1) the majority of energy dissipation is due to shear (i.e., the frictional dissipation) and (2) some energy dissipation is due to

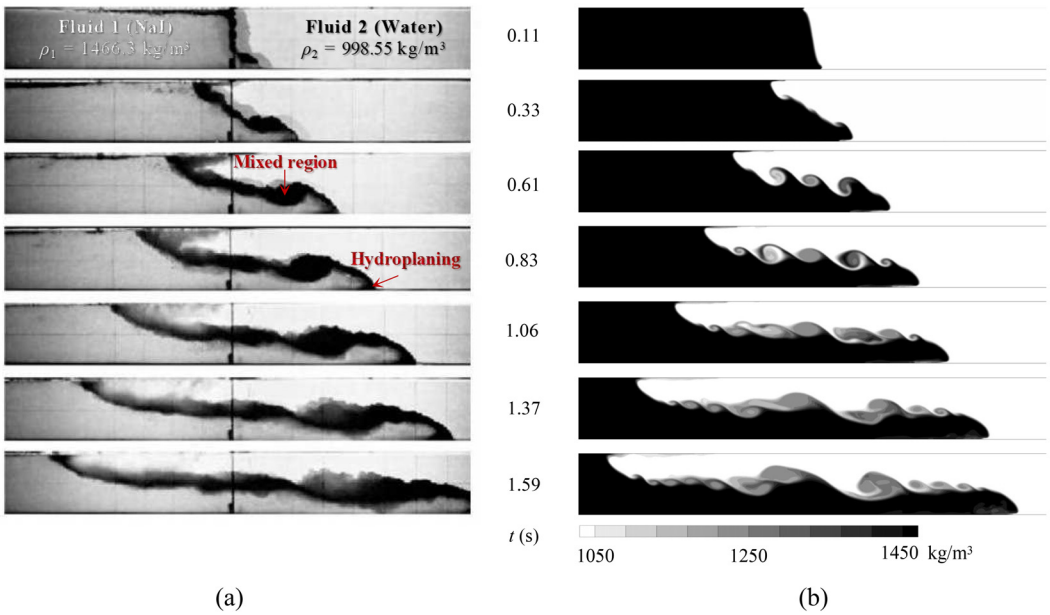

FIG. 5. Snapshots of the fluids' movement and mixing processes: (a) lock-exchange experiment and (b) LES case B ($Sc = 0.1$). Adapted from Ref. 80.

overcoming the gravity work to transfer densities. Interestingly, the dissipated energy is always greater than the kinetic energy as the gravity currents evolve. Figure 9 presents contours of the kinetic energy distribution per unit length in the y direction. The kinetic energy within the mixing region is dissipated, resulting in a very low kinetic energy region within a small range between areas of high kinetic energy, which also signifies the turbulent mixing region. It is of great importance to consider the transport dynamics of the density[98] when predicting the migration of submarine turbidity currents along the seabed.

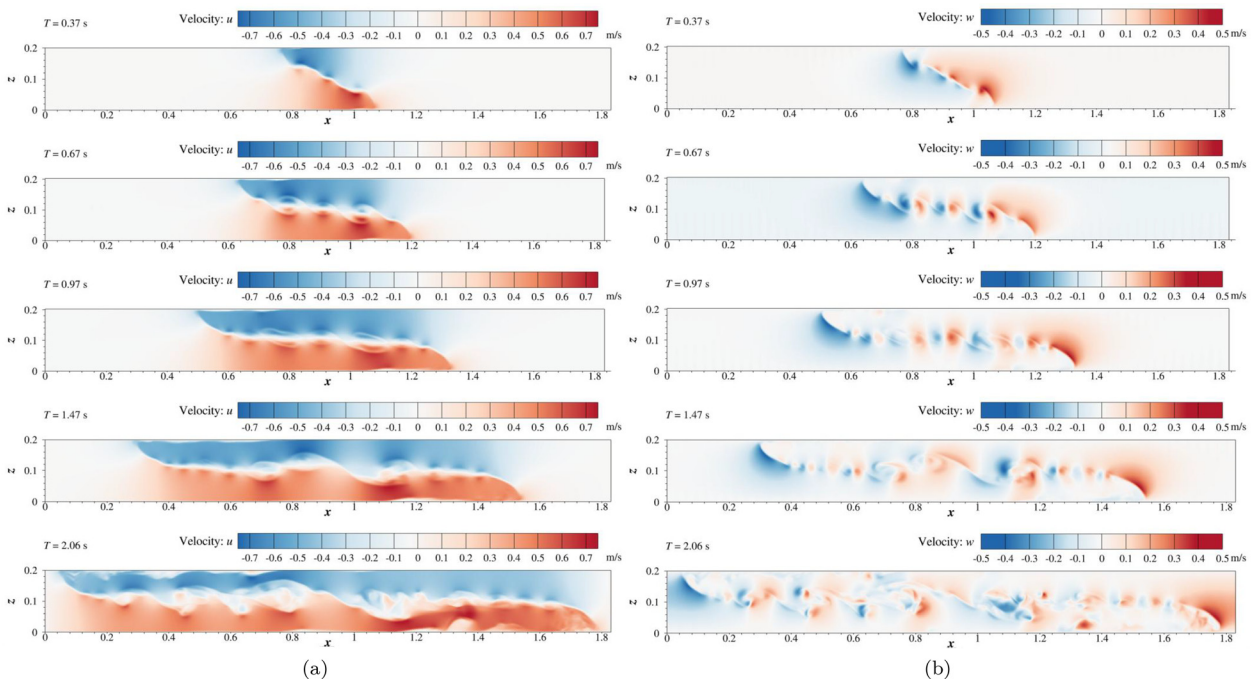

FIG. 6. Contours of the fluid velocity at selected instants in time: (a) streamwise velocity and (b) vertical velocity.

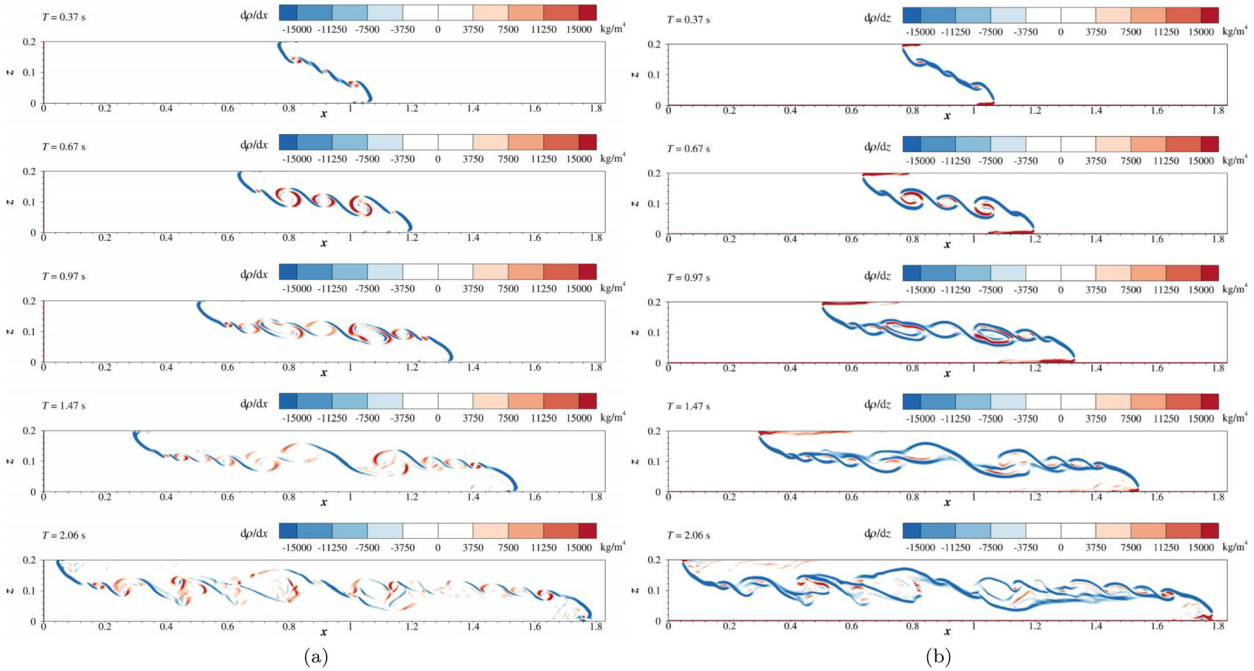

FIG. 7. Contours of the density gradient at selected instants in time: (a) streamwise gradients and (b) vertical gradients.

Large-volume, long-distance, and high-velocity migration mechanism of a high-density turbidity current are driven by the two mechanisms as illustrated in Fig. 10. First, in the turbulent mixing region along the top of the high-density turbidity current, the countercurrent of the low-density fluid causes entrainment of it due to the formation of a strong shear layer, the formation of turbulence structures [Figs. 10(e) and 10(f)] which promote enhanced turbulent mixing. Turbulent mixing promotes a gradual increase in the volume of the turbidity current, yet the heavy fluid remains near the bed and maintains its high velocity. Second, a secondary mixing region occurs near the head and at the bottom of the high-density turbidity current, causing intrusion of low-density ambient water thereby forming a thin water cushion, the so-called hydroplaning [Figs. 10(a) and 10(d)]. This water cushion separates the head of the submarine turbidity current from the seabed, reducing the friction between the current and seabed, which promotes the long-distance migration of the submarine turbidity current. At the same time, as the water cushion continues to thicken, this part of the water body mixes upward with the head of the turbidity current caused by vertical velocities, gradually forming some small eddies, reducing the density of the head of the turbidity current, and gradually disintegrating the head. Past studies[96–99] have demonstrated the occurrence of hydroplaning when the developing hydrodynamic pressure P_f on the bottom of the submarine turbidity current is larger than the load P_d of the head of the submarine turbidity current. Figures 10(b) and 10(c) present the equations for assessing whether the hydroplaning phenomenon occurs in past studies[65] without considering density mixing (b) and in our study considering density mixing (c), respectively. Compared with past studies, our study results in a smaller P_d and larger P_f. Therefore, our study supports the fact that when ignoring density mixing underestimates P_f and overestimates P_d, suggesting that past studies may have underestimated the effect of the hydroplaning phenomena on the speed of the turbidity current and its devastating impact on engineered subsea structures such as pipelines.

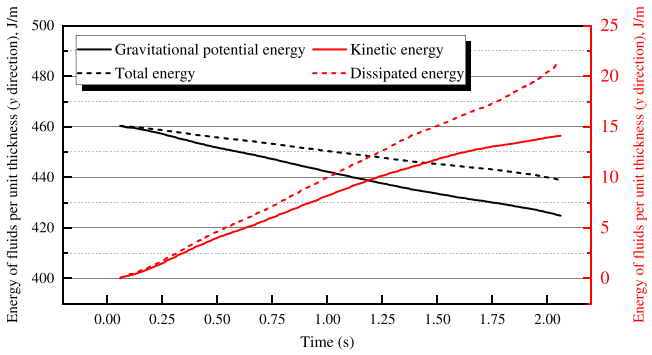

FIG. 8. Energies (i.e., total energy, potential energy, kinetic energy, and dissipated energy) per unit length as a function of time.

C. Impact of the high-density turbidity current on a pair of parallel suspended pipes

With the significant increase in the demand for submarine pipelines or cables, co-hosting of multiple pipelines in close proximity is increasingly common in order to meet the demands of the growth of offshore activities.[43,100–103] For instance, the "Nord Stream 2" pipeline

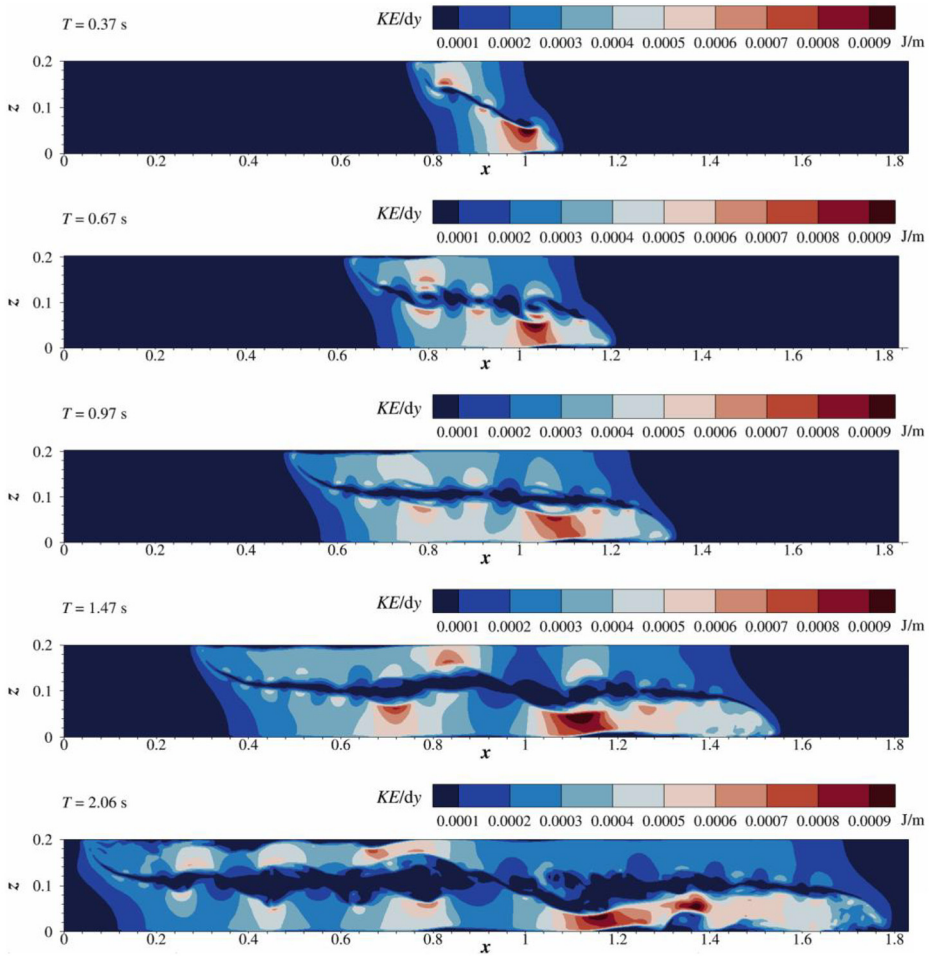

FIG. 9. Contours of the kinetic energy gradient per unit length at selected instants in time.

was constructed in parallel to the "Nord Stream 1" pipeline through the Baltic Sea to transport natural gas.[101,102] The hydrodynamics around parallel pipelines is very complex, and during their long-term service, these may be exposed to extreme natural disasters, such as turbidity currents. It is necessary to assess the survivability of a pair of parallel suspended pipes subjected to submarine turbidity currents including their realistic fully-turbulent flow characteristics. Figure 11 sketches the setup of a pair of parallel suspended pipes within the computational domain. The location of the first pipe is fixed for all simulations, while the streamwise (i.e., *x*-) position of the second pipe varies, resulting in a varying spacing *S* between the parallel pipes. The diameter of the pipes is 0.02 m, while both pipes are located 0.01 m (the span height is 0.5*D*, which is very common as found from *in situ* investigation by Huang *et al.*[104]) away from the seabed. Details regarding the locations of the pipes as well as the spacing are shown in Table II. The hollow box surrounded by black lines in Fig. 12 presents the range of positions of the two pipes for different simulation cases. The height, flow direction, and velocity of the turbidity flow through the hollow box range remain relatively constant over time. Therefore, this specific area can be chosen for analyzing the impact of turbidity flow on pipes with varying streamwise spacing.

Figure 13 presents the methodology of calculating drag F_D and lift forces F_L acting on a pipe by using differential pressure and friction forces,[105] where p_d represents the dynamic pressure (i.e., the static pressure is removed) in the current LES method. w and u represent the vertical and streamwise velocities, which are interpolated from the Cartesian grid around the pipe onto the blue circle; p_d represents the dynamic pressure on the pipe [i.e., $p_d(i,j,k) = p(i,j,k) - \sum_k^{z_0/dz} \rho(i,j,k) \cdot g \cdot dz$]; f represents the frictional stress on the pipe [i.e., $f = (u \cdot \cos\beta - w \cdot \sin\beta)/dx \cdot \rho \cdot \nu \cdot \frac{\pi D}{N} \cdot dy$, where $N = 20$ is the number of locations taken over the circumference of the pipe]; f_x and f_z represent the frictional stresses on the pipe in the streamwise and vertical directions, respectively; p_x and p_z represent the dynamic pressures on the pipe in the streamwise and vertical directions, respectively; dx and dz represent the grid sizes in streamwise and vertical directions, respectively; and F_x and F_z represent the streamwise and vertical forces on the pipe, which are essentially the drag or lift forces, respectively.

Figure 14 presents the turbidity current's impact forces on pipe 1 as a function of time and for various spacings between pipe 1 and pipe 2. The peak drag force (the amplitude as well as the corresponding time) of the high-density turbidity current on pipe 1 is hardly affected

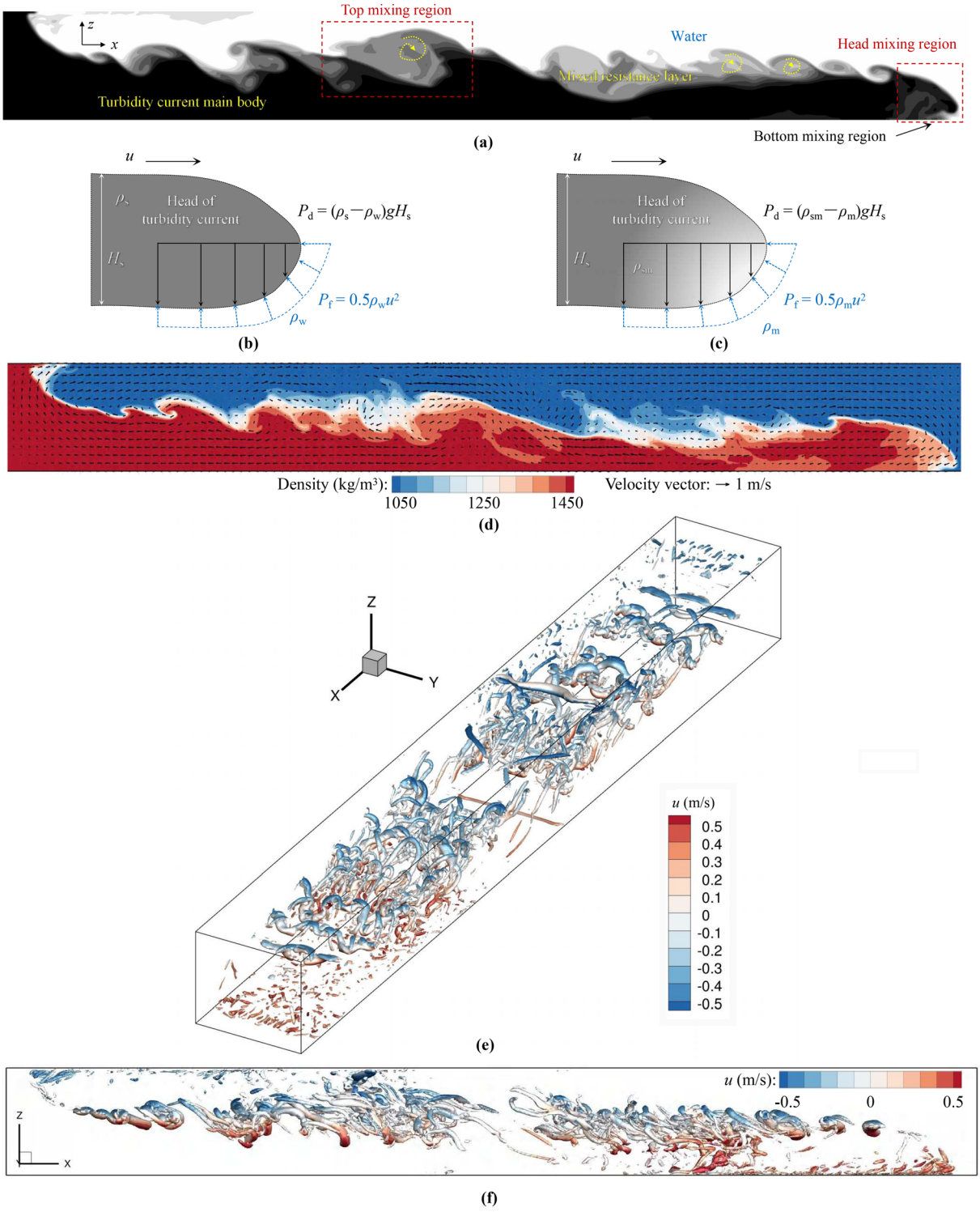

FIG. 10. Illustration of the dynamics of a high-density submarine turbidity current: (a) overall evolutionary process, (b) hydroplaning characteristics assessment of the turbidity current head without considering density evolution process, (c) hydroplaning characteristics assessment of the turbidity current head with considering density evolution process, (d) velocity vector (refer to Fig. 6) and density contour, (e) visualization of Q criterion with an iso-surface of 400 s^{-2} using streamwise velocity ($t = 2$ s), and (f) side view of Q criterion with an iso-surface of 400 s^{-2} using streamwise velocity ($t = 2$ s).

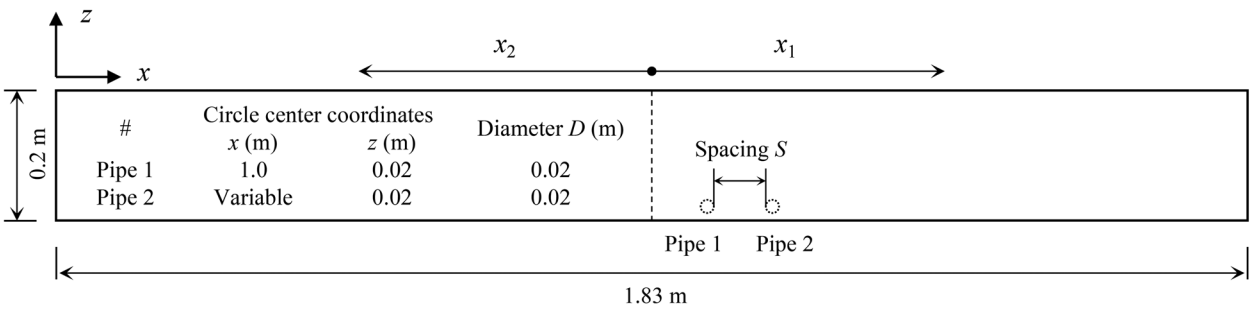

FIG. 11. Sketch of the simulated pair of parallel suspended pipes with different streamwise spacings.

by the location of pipe 2. However, a maximum difference of approximately 1.6 times (between the spacing of 2*D* and *8D* cases) is observed in the later stage (when the drag is stabilized). The highest peaks in the lift force are observed in the 1*D and 2D* cases, which also show weaker fluctuations (both in amplitude and frequency) in the later stage compared to those in the larger spacing cases. The effect that pipe 2 imposed on the lift force of pipe 1 can be ignored when the streamwise spacing is larger than 3*D*. The lift force oscillation exhibits some asymmetry which is owing to the fact that the flow is accelerated between pipe and bottom.

Figure 15 presents the turbidity current's impact forces on pipe 2 as a function of time. It is found that both the drag force and the lift force of the high-density turbidity current acting on pipe 2 is significantly influenced by the presence of and distance to pipe 1, exhibiting a completely different pattern from those shown in Fig. 14. Figure 16 presents peak drag forces acting on pipe 2 (and ratios of the first peak drag force on pipe 2 to the peak drag force on a single pipe) for various pipe spacings. The peak drag force on pipe 2 first increases, reaching its peak at 8*D* spacing, then decreases, and, finally, tends to be constant with increasing spacing between the two pipes. Due to the presence of pipe 1, the maximum drag force acting on pipe 2 is reduced by 54% compared with that on a single pipe. At the same time, the lift force on pipe 2 is also affected; however, the amplitude of the lift force is smaller than the drag force. Noticeably, the drag and lift forces on pipe 2 oscillate when the spacing between two pipes exceeds 2*D*. Such force vibration may cause pipe fatigue which should be taken into account during the engineering design.

TABLE II. Location of a pair of parallel suspended pipes with different streamwise spacings for all simulated cases.

Run	x_1(m)	z_1(m)	x_2(m)	z_2(m)	S(m)	S/D
1	1.00	0.02	1.04	0.02	0.02	1
2	1.00	0.02	1.06	0.02	0.04	2
3	1.00	0.02	1.08	0.02	0.06	3
4	1.00	0.02	1.10	0.02	0.08	4
5	1.00	0.02	1.12	0.02	0.10	5
6	1.00	0.02	1.14	0.02	0.12	6
7	1.00	0.02	1.16	0.02	0.14	7
8	1.00	0.02	1.18	0.02	0.16	8
9	1.00	0.02	1.20	0.02	0.18	9
10	1.00	0.02	1.22	0.02	0.20	10
11	1.00	0.02	1.24	0.02	0.22	11
12	1.00	0.02	1.26	0.02	0.24	12
13	1.00	0.02	1.28	0.02	0.26	13
14	1.00	0.02	1.30	0.02	0.28	14
15	1.00	0.02	1.32	0.02	0.30	15

The quantitative results of all simulated cases demonstrate that the dynamic pressure contributes more than 99% to the drag and lift forces, which is significantly different from previous studies on the impact of high-viscosity non-Newtonian fluids with special reference to submarine landslides on pipelines.[105] The dynamic pressure is dependent on the variation of the velocity and density fields. Figure 17(a) presents contours of the densities of the two fluids around the two pipes with different spacing (i.e., 1*D*, 4*D*, 8*D*, 11*D*, and *15D*), corresponding to the time step when the peak drag force on pipe 2 occurs. At this instant, the turbidity current that has bypassed pipe 1 has just reached pipe 2 for all cases. When the streamwise spacing between the two pipes is small (i.e., 1*D* and *2D*), the turbidity current separates at the upstream pipe and bypasses pipe 2, hence trapping low-momentum, low-density fluid upstream of pipe 2, which results in smaller peak impact forces on pipe 2. Figure 17(b) presents the contours of the densities of fluids around the two pipes with different spacing at the time step of 1.5 s when fluids have long passed pipe 2. Clearly, when the spacing between the two pipes is small, there is still low-density fluid between the pipes which results in high drag forces on pipe 1 in the stable regime. The evolution of the density of the turbidity current around two pipes enhances the mixing of the two fluids, and hence, the distribution of the density field around pipes is quite complex and differs from past studies of flow over pipes in which constant density was assumed or where the transport of fluid density was not considered.

Figure 18 presents contours of the streamwise and vertical velocities of the high-density fluid around the pair of suspended pipes at different spacings at the instant when the peak drag force is acting on pipe 2. It is found that the wake of pipe 1 is diminished when pipe 2 is close to pipe 1 (approximately at $S \leq 2D$). As the spacing between the two pipes increases, the turbidity current passing pipe 1 starts to generate "von Karman-type" vortex streets resulting in an oscillatory wake flow downstream of pipe 1. It is noteworthy that the seabed (i.e., the bottom boundary) constrains that wake in the vertical direction. The wake generated by pipe 1 enhances the transport and mixing of the fluids (shown in Fig. 17). At close spacing, the lighter fluid is

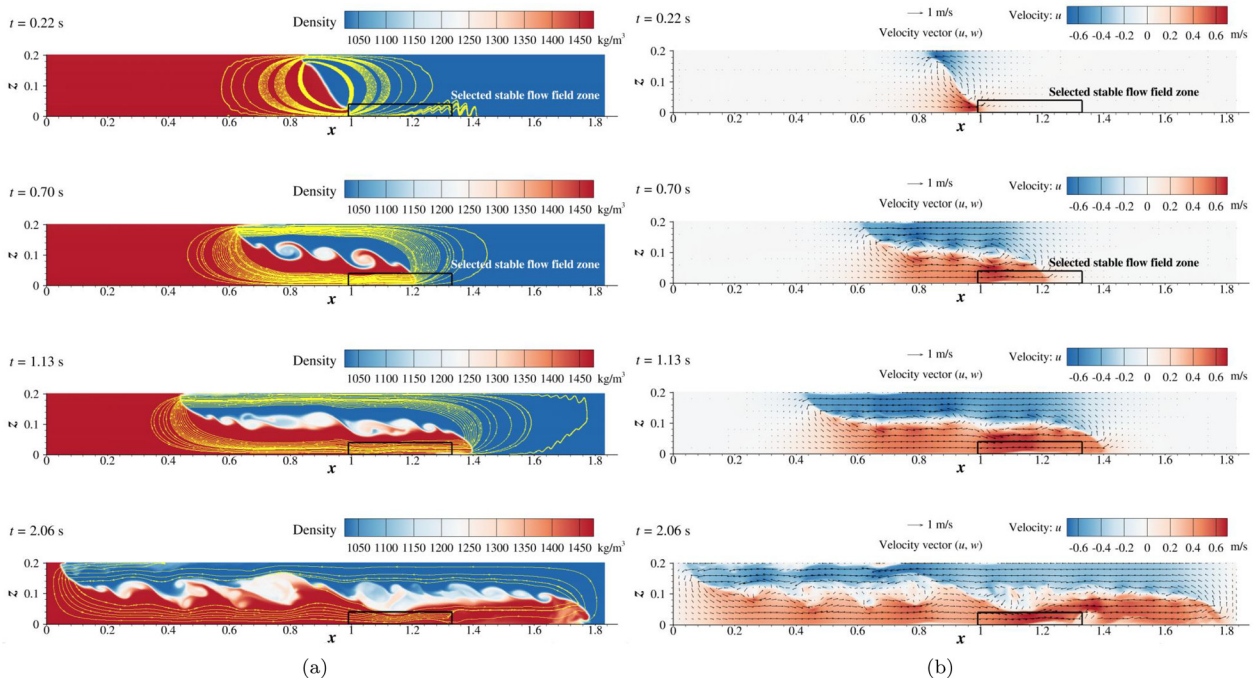

FIG. 12. Contours of flow fields of the submarine turbidity current and water at selected instants in time: (a) density and streamlines and (b) streamwise velocity and velocity vectors.

entrapped between pipes. The critical spacing, which is when the maximum drag force on pipe 2 occurs, is around 8*D* and mixed high-density fluid impacts on pipe 2. Beyond 8*D*, the effect of turbulent mixing due to entrainment of lighter fluid into the wake gradually reduces the peak force on pipe 2 and reaches a steady state (defined as no further increase in the drag force acting on pipe 2). It can be predicted that the effect of pipe 1 on pipe 2 can be neglected when the two pipes are separated beyond 15*D*. The highest streamwise velocity is always observed between pipe 2 and the seabed, while the highest vertical velocity is always found over the upper left area of pipe 2, which is when the kinetic energy around pipe 2 is maximum. Figure 19 presents contours of the kinetic energy (per unit length in the *y* direction) at the instant of the peak drag force on pipe 2. Due to the effects of the narrow gap between bottom boundary and pipe, the turbidity current below the pipes is accelerated, resulting in a large gradient of kinetic energy. Together, the streamwise velocity and density cause significant variation in the impact forces on pipe 2. Figure 20 presents contours of the dynamic pressure around the two pipes with

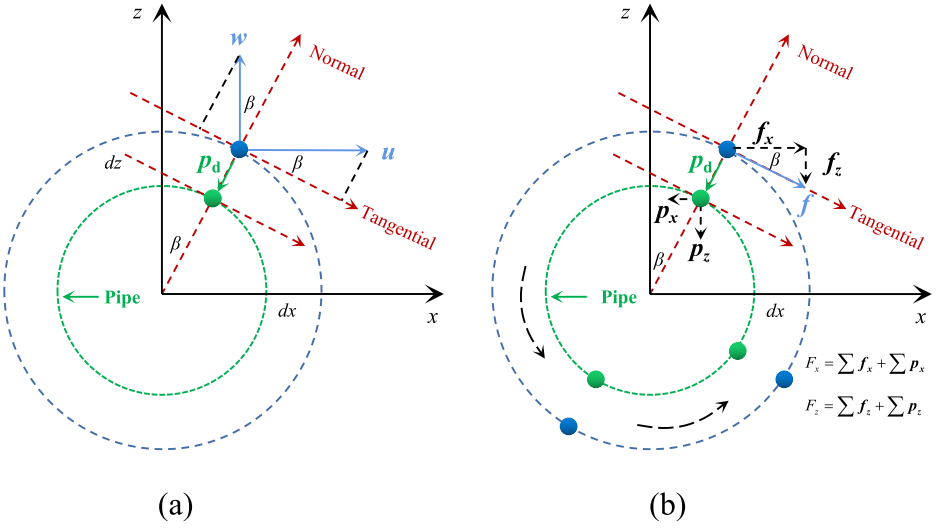

FIG. 13. Methodology of calculating impact forces (i.e., the drag and lift forces) on a pipe by using the differential pressure and friction force.

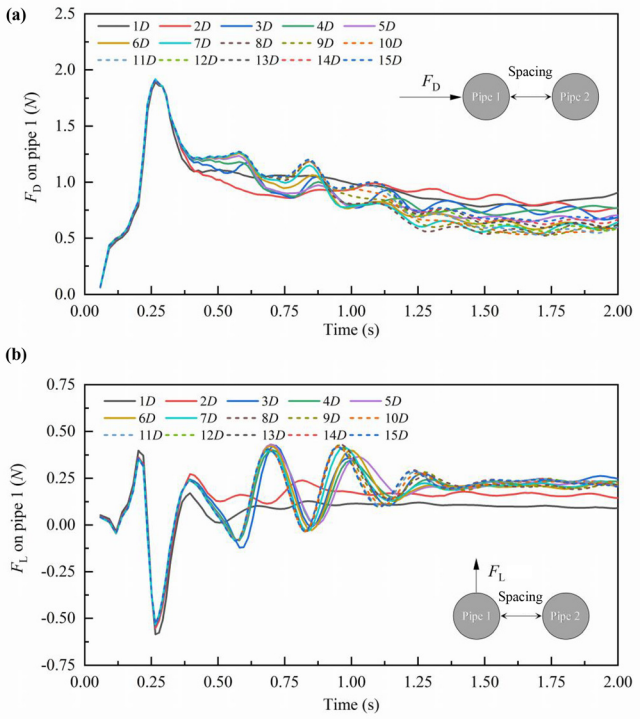

FIG. 14. Submarine turbidity current's impact forces on pipe 1 at different streamwise spacings: (a) drag force F_{D1} as a function of time and (b) lift force F_{L1} as a function of time.

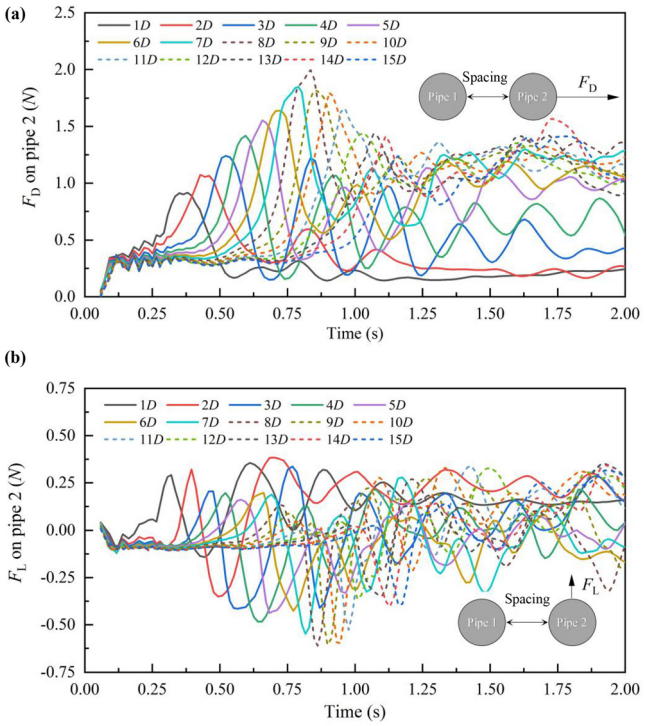

FIG. 15. Submarine turbidity current's impact forces on pipe 2 at different streamwise spacings: (a) drag force F_{D2} as a function of time and (b) lift force F_{L2} as a function of time.

different streamwise spacings at the instant of the peak drag force on pipe 2. The acting position of the maximum dynamic pressure on pipe 2 gradually moves upward, and the magnitude of the dynamic pressure first increases and then decreases with increasing streamwise spacing between the two pipes, demonstrating a pattern similar to the change in velocity, which leads to the force pattern of pipe 2, as shown in Figs. 15 and 16.

Based on the simulations and discussion above, it can be concluded that the streamwise spacing between two pipes with less than 2*D* offers the optimum protection for pipe 2. Although the peak impact forces on pipe 2 are still close to or lower than the peak impact forces on pipe 1, the vibration of the impact forces with increasing streamwise spacing between the two pipes needs to be considered in the pipeline design stage too. Therefore, it is recommended that the streamwise spacing between two pipes should be less than 2*D*. This significantly increases the difficulty of construction, so it is suggested that the simultaneous laying of two pipes may be a better option.

IV. SUMMARY AND CONCLUSIONS

Large-eddy simulations of the flow and fluid density transport are employed to investigate the evolution of a high-density turbidity current in ambient water and its impact on a pair of parallel suspended pipes. The LES method is validated to provide good accuracy in head velocities of the high and low-density fluids, which is in good agreement with data of Lowe *et al.*'s non-Boussinesq lock-exchange experiment.[80]

The effect of the subgrid scale Schmidt number *Sc* (i.e., the diffusion coefficient) on the head velocity and density mixing process during the migration of a high-density and low-viscosity turbidity current is insignificant in the LES method used here. High- and low-density fluids with opposite direction of motion generate vortices in the turbulent shear layer (or the mixed resistance layer) to achieve fluid mixing, resulting in energy loss. The shear layer separates the ambient water at the top from the main body of the high-density turbidity current at the

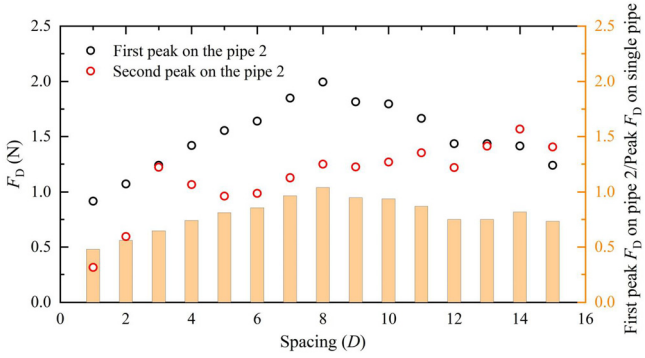

FIG. 16. Peak drag forces on pipe 2 (and ratios of the first peak drag force on pipe 2 to the peak drag force on single pipe) as functions of the streamwise spacing between the two pipes.

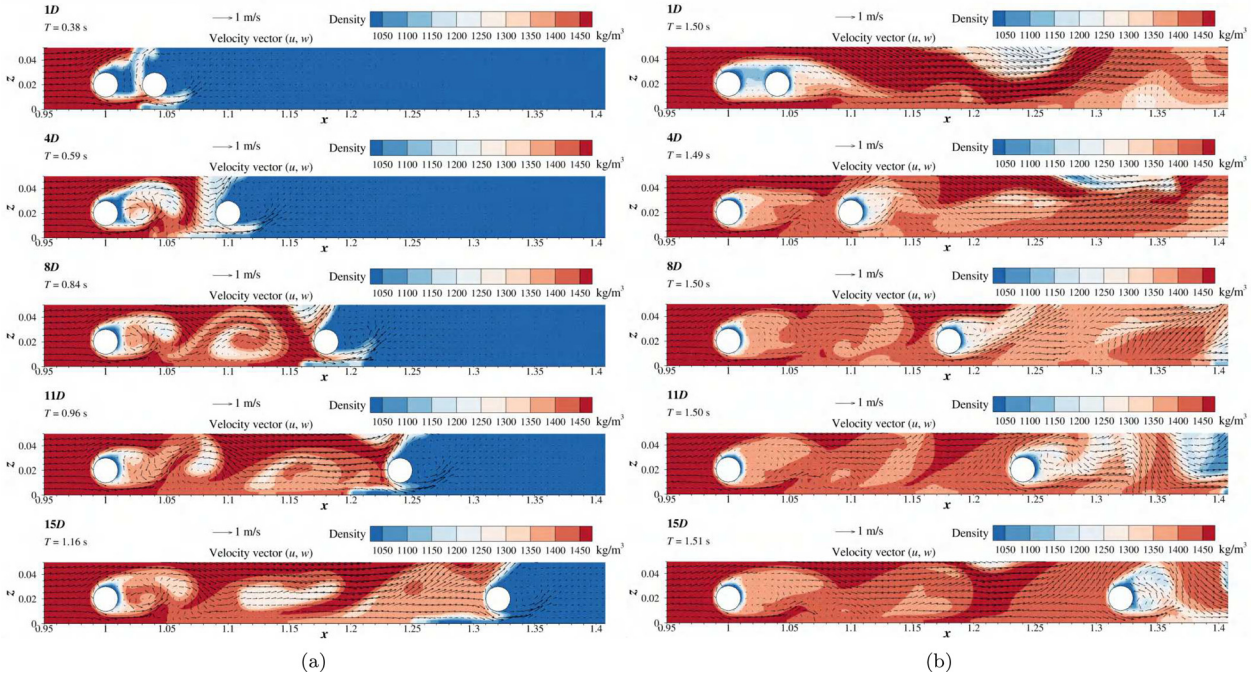

FIG. 17. Contours of the density of the two fluids around a pair of parallel suspended pipes at different spacing: (a) instant of peak drag force on pipe 2 and (b) instant(s) of stable drag force on pipe 2 (i.e., 1.5s).

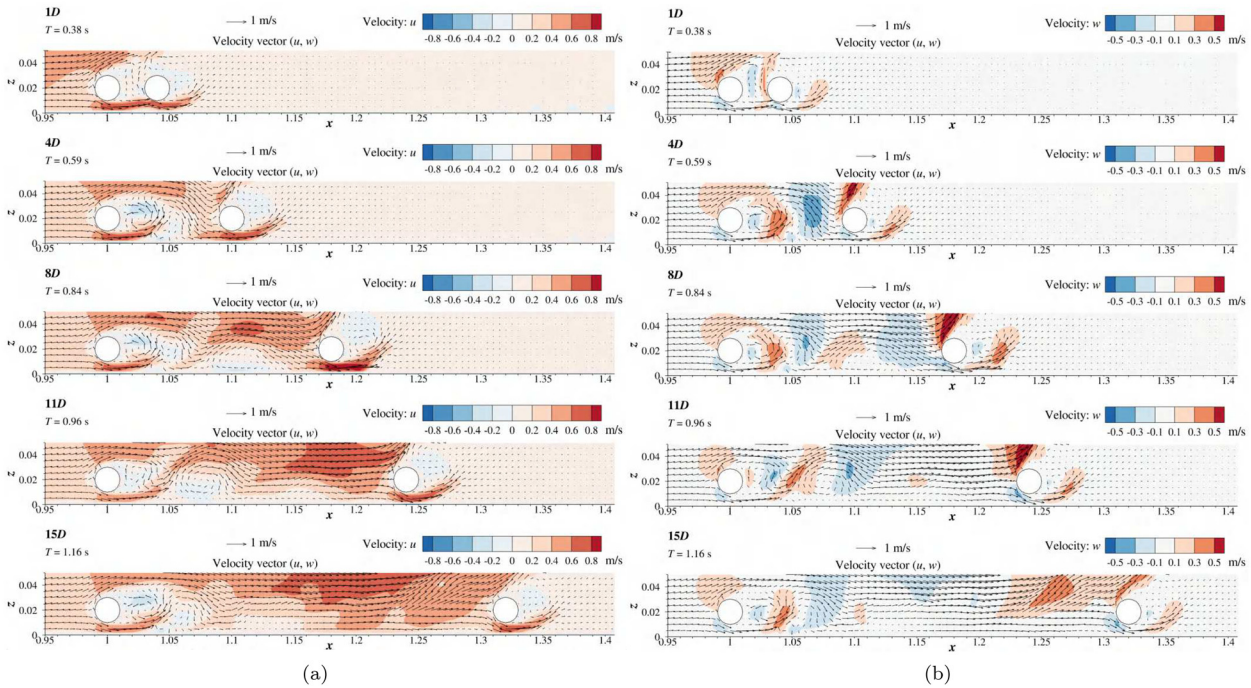

FIG. 18. Contours of the streamwise velocity of the two fluids around a pair of parallel suspended pipes at different streamwise spacing at the instant of peak drag force on pipe 2: (a) streamwise velocity and (b) vertical velocity.

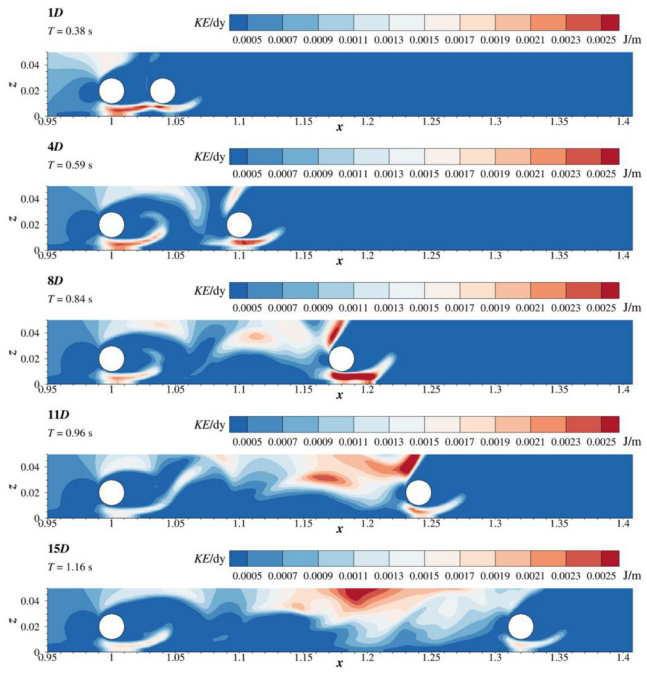

FIG. 19. Contours of the kinetic energy distribution per unit length in the *y* direction around a pair of parallel suspended pipes at different streamwise spacing at the instant of peak drag force on pipe 2.

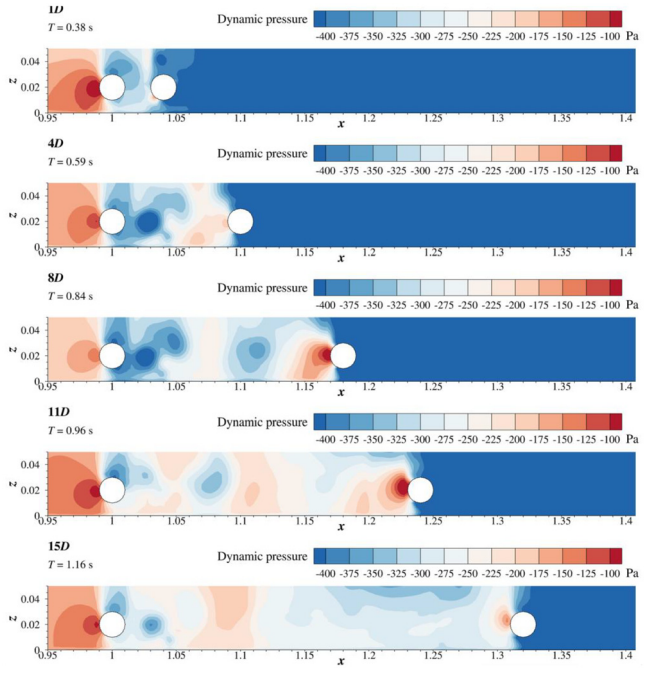

FIG. 20. Contours of the dynamic pressure around a pair of parallel suspended pipes at different streamwise spacing at the instant of peak drag force on pipe 2.

bottom to maintain the kinetic energy of the main body and only gradually entrains ambient fluid and, hence, maintains the large-volume characteristics of the turbidity current. Low-density ambient water close to the bottom boundary intrudes into the high-density turbidity current, forming a thin water cushion, the so-called hydroplaning, and separates the head of the turbidity from the seabed, thereby reducing the friction of the heavy fluid and supporting its long-distance and high-velocity transport characteristics. This study suggests that ignoring density mixing underestimates the hydrodynamic force, P_f, and overestimates the weight (load), P_d, which shows that past studies may have underestimated the possibility and risk of the hydroplaning phenomena.

Further, a pair of parallel suspended pipes with different spacings impacted by a turbidity current has been investigated. The results show that the peak drag force on the upstream pipe (pipe 1) is almost unaffected by the presence of the downstream pipe (pipe 2); however, in the stable drag force regime, the drag force is approximately 1.6 times greater for closely spaced pipes ($S/D < 2$) than for widely spaced pipes ($S/D > 2$). The peak drag force on pipe 2 first increases with increasing pipe spacing, attains a peak at $S/D = 8$, and then decreases again with increasing streamwise spacing between the two pipes. The drag and lift forces on pipe 2 oscillate when the streamwise spacing between two pipes exceeds 2*D*. The "von Karman" vortex street generated behind pipe 1 enhances the transport of the head's density causing a complex distribution of the density field of the turbidity current around pipes. In parallel, the combined effect of intensity and influence of the turbulent wake on pipe 2 become strong with increasing streamwise spacing between the two pipes, resulting in a more unstable velocity field acting on pipe 2. In addition, the turbidity current bypassing pipes is accelerated due to the effects of the bottom boundary leading to an asymmetric distribution of the lift force. When the streamwise spacing between two pipes is less than 2*D*, optimum protection of pipe 2 is achieved. This study provides invaluable insight into the evolution mechanism of high-density submarine turbidity current and its impact forces on a pair of parallel suspended pipes.

ACKNOWLEDGMENTS

Financial support for this work is provided by the National Natural Science Foundation of China (42277138); the Opening fund of State Key Laboratory of Coastal and Offshore Engineering (Dalian University of Technology) (LP2310); the Opening fund of State Key Laboratory of Geohazard Prevention and Geoenvironment Protection (Chengdu University of Technology) (SKLGP2023K001); the Shandong Provincial Natural Science Foundation (ZR2020YQ29); the Department of Civil, Environmental and Geomatic Engineering at University College London; and the Shandong Provincial Key Laboratory of Marine Environment and Geological Engineering at Ocean University of China.

AUTHOR DECLARATIONS

Conflict of Interest

The authors have no conflicts to disclose.

Author Contributions

Xingsen Guo: Data curation (equal); Formal analysis (equal); Methodology (equal); Validation (equal); Writing – original draft (equal). **Qianyu Luo:** Software (equal); Validation (equal); Writing –

original draft (equal). **Thorsten Stoesser:** Funding acquisition (equal); Project administration (equal); Resources (equal); Software (equal); Supervision (equal); Writing – review & editing (equal). **Arthur Hajaali:** Software (supporting); Writing – review & editing (supporting). **Xiaolei Liu:** Funding acquisition (equal); Investigation (equal); Project administration (equal); Resources (equal); Writing – review & editing (equal).

DATA AVAILABILITY

The data that support the findings of this study are available from the corresponding authors upon reasonable request.

REFERENCES

[1]J. Xu, "Turbidity current research in the past century: An overview," Period. Ocean Univ. China **44**, 98–105 (2014).
[2]G. Shanmugam and Y. Wang, "The landslide problem," J. Palaeogeogr. **4**, 109–166 (2015).
[3]X. Liu, J. Sun, Y. Lu, and X. Guo, "Control of ambient fluid on turbidity current evolution: Mechanisms, feedbacks and influencing factors," Geosyst. Geoenviron. **2**, 100214 (2023).
[4]R. G. Walker, "Deep-water sandstone facies and ancient submarine fans: Models for exploration for stratigraphic traps," AAPG Bull. **62**, 932–966 (1978).
[5]C. Pirmez and J. Imran, "Reconstruction of turbidity currents in amazon channel," Mar. Pet. Geol. **20**, 823–849 (2003).
[6]R. Ouillon, C. Kakoutas, E. Meiburg, and T. Peacock, "Gravity currents from moving sources," J. Fluid Mech. **924**, A43 (2021).
[7]X. Guo, N. Fan, Y. Liu, X. Liu, Z. Wang, X. Xie, and Y. Jia, "Deep seabed mining: Frontiers in engineering geology and environment," Int. J. Coal Sci. Technol. **10**, 23 (2023).
[8]J. S. Salinas, S. Balachandar, S. L. Zúñiga, M. Shringarpure, J. Fedele, D. Hoyal, and M. Cantero, "On the definition, evolution, and properties of the outer edge of gravity currents: A direct-numerical and large-eddy simulation study," Phys. Fluids **35**, 016610 (2023).
[9]P. D. Komar, "The channelized flow of turbidity currents with application to Monterey deep-sea fan channel," J. Geophys. Res. **74**, 4544–4558, https://doi.org/10.1029/JC074i018p04544 (1969).
[10]G. Parker, Y. Fukushima, and H. M. Pantin, "Self-accelerating turbidity currents," J. Fluid Mech. **171**, 145–181 (1986).
[11]J. Locat and H. J. Lee, "Submarine landslides: Advances and challenges," Can. Geotech. J. **39**, 193–212 (2002).
[12]J. J. Hance, "Submarine slope stability," Ph.D. thesis, University of Texas at Austin, 2003.
[13]P. Jeanjean, E. Liedtke, E. Clukey, K. Hampson, T. Evans *et al.*, "An operator's perspective on offshore risk assessment and geotechnical design in geohazard-prone areas," in *Proceedings of the Offshore Technology Conference* (2005), pp. 115–143.
[14]X. Liu, Y. Wang, H. Zhang, and X. Guo, "Susceptibility of typical marine geological disasters: An overview," Geoenviron. Disasters **10**, 10 (2023).
[15]P. J. Talling, L. A. Amy, R. B. Wynn, G. Blackbourn, and O. Gibson, "Evolution of turbidity currents deduced from extensive thin turbidites: Marnoso arenacea formation (miocene), italian apennines," J. Sediment. Res. **77**, 172–196 (2007).
[16]W. Schneeberger, "Turbidity currents, a new concept in sedimentation and its application to oil exploration," Mines Mag. **45**, 42–62 (1955).
[17]P. Weimer, R. M. Slatt, R. Bouroullec *et al.*, *Introduction to the Petroleum Geology of Deepwater Setting* (AAPG/Datapages Tulsa, 2007), Vol. 111.
[18]E. Meiburg and B. Kneller, "Turbidity currents and their deposits," Annu. Rev. Fluid Mech. **42**, 135–156 (2010).
[19]D. Bell, E. L. Soutter, Z. A. Cumberpatch, R. A. Ferguson, Y. T. Spychala, I. A. Kane, and J. T. Eggenhuisen, "Flow-process controls on grain type distribution in an experimental turbidity current deposit: Implications for detrital signal preservation and microplastic distribution in submarine fans," Depositional Rec. **7**, 392–415 (2021).
[20]A. Zakeri, K. Høeg, and F. Nadim, "Submarine debris flow impact on pipelines—Part I: Experimental investigation," Coastal Eng. **55**, 1209–1218 (2008).
[21]M. Shringarpure, M. I. Cantero, and S. Balachandar, "Dynamics of complete turbulence suppression in turbidity currents driven by monodisperse suspensions of sediment," J. Fluid Mech. **712**, 384–417 (2012).
[22]X.-s. Guo, T.-k. Nian, Z.-t. Wang, W. Zhao, N. Fan, and H.-b. Jiao, "Low-temperature rheological behavior of submarine mudflows," J. Waterw., Port, Coastal, Ocean Eng. **146**, 04019043 (2020).
[23]Z. Tian, Y. Jia, J. Chen, J. P. Liu, S. Zhang, C. Ji, X. Liu, H. Shan, X. Shi, and J. Tian, "Internal solitary waves induced deep-water nepheloid layers and seafloor geomorphic changes on the continental slope of the northern south china sea," Phys. Fluids **33**, 053312 (2021).
[24]S.-K. Hsu, J. Kuo, L. Chung-Liang, T. Ching-Hui, W.-B. Doo, C.-Y. Ku, and J.-C. Sibuet, "Turbidity currents, submarine landslides and the 2006 Pingtung earthquake off SW Taiwan," Terr., Atmos. Oceanic Sci. **1**, 1229 (2008).
[25]T.-k. Nian, X.-s. Guo, N. Fan, H.-b. Jiao, and D.-y. Li, "Impact forces of submarine landslides on suspended pipelines considering the low-temperature environment," Appl. Ocean Res. **81**, 116–125 (2018).
[26]X. Guo, T. Stoesser, C. Zhang, C. Fu, and T. Nian, "Effect of opening and wall boundaries on CFD modeling for submarine landslide-ambient water-pipeline interaction," Appl. Ocean Res. **126**, 103266 (2022).
[27]M. G. Wells and R. M. Dorrell, "Turbulence processes within turbidity currents," Annu. Rev. Fluid Mech. **53**, 59–83 (2021).
[28]K. Chikita, "A field study on turbidity currents initiated from spring runoffs," Water Resour. Res. **25**, 257–271, https://doi.org/10.1029/WR025i002p00257 (1989).
[29]C. Gong, Y. Wang, W. Zhu, W. Li, Q. Xu, and J. Zhang, "The central submarine canyon in the Qiongdongnan basin, northwestern south China sea: Architecture, sequence stratigraphy, and depositional processes," Mar. Pet. Geol. **28**, 1690–1702 (2011).
[30]W. Ding, J. Li, J. Li, Y. Fang, and Y. Tang, "Morphotectonics and evolutionary controls on the pearl river canyon system, south china sea," Mar. Geophys. Res. **34**, 221–238 (2013).
[31]M. Azpiroz-Zabala, M. Cartigny, E. J. Sumner, M. Clare, P. J. Talling, D. R. Parsons, and C. Cooper, "A general model for the helical structure of geophysical flows in channel bends," Geophys. Res. Lett. **44**, 11932–11941, https://doi.org/10.1002/2017GL075721 (2017).
[32]X. Liu, Y. Lu, H. Yu, L. Ma, X. Li, W. Li, H. Zhang, and C. Bian, "*In-situ* observation of storm-induced wave-supported fluid mud occurrence in the subaqueous yellow river delta," J. Geophys. Res.: Oceans **127**, e2021JC018190, https://doi.org/10.1029/2021JC018190 (2022).
[33]M. A. Hampton, "The role of subaqueous debris flow in generating turbidity currents," J. Sediment. Res. **42**, 775–793 (1972).
[34]M. M. Hotta, M. S. Almeida, D. T. Pelissaro, J. R. M. da S. de Oliveira, S. Tibana, and R. G. Borges, "Centrifuge tests for evaluation of submarine-mudflow hydroplaning and turbidity currents," Int. J. Phys. Modell. Geotech. **20**, 239–253 (2020).
[35]M. R. Oshaghi, H. Afshin, and B. Firoozabadi, "Experimental investigation of the effect of obstacles on the behavior of turbidity currents," Can. J. Civ. Eng. **40**, 343–352 (2013).
[36]Z. F. Haza, I. S. H. Harahap, and L. M. Dakssa, "Experimental studies of the flow-front and drag forces exerted by subaqueous mudflow on inclined base," Nat. Hazards **68**, 587–611 (2013).
[37]O. E. Sequeiros, R. Mosquera, and F. Pedocchi, "Internal structure of a self-accelerating turbidity current," J. Geophys. Res.: Oceans **123**, 6260–6276, https://doi.org/10.1029/2018JC014061 (2018).
[38]G. H. Keulegan, *Twelfth Progress Report on Model Laws for Density Currents*, The Motion of Saline Fronts in Still Water Vol. 5831 (U.S. Department of Commerce, National Bureau of Standards, 1958).
[39]R. Kelly, R. Dorrell, A. Burns, and W. McCaffrey, "The structure and entrainment characteristics of partially confined gravity currents," J. Geophys. Res.: Oceans **124**, 2110–2125, https://doi.org/10.1029/2018JC014042 (2019).
[40]Z. He, D. Han, Y.-T. Lin, R. Zhu, Y. Yuan, and P. Jiao, "Propagation, mixing, and turbulence characteristics of saline and turbidity currents over rough and permeable/impermeable beds," Phys. Fluids **34**, 066604 (2022).

[41]T. B. Benjamin, "Gravity currents and related phenomena," J. Fluid Mech. **31**, 209–248 (1968).
[42]V. Birman, J. Martin, and E. Meiburg, "The non-Boussinesq lock-exchange problem. Part 2. High-resolution simulations," J. Fluid Mech. **537**, 125–144 (2005).
[43]L. Zhao, C.-H. Yu, and Z. He, "Numerical modeling of lock-exchange gravity/turbidity currents by a high-order upwinding combined compact difference scheme," Int. J. Sediment Res. **34**, 240–250 (2019).
[44]M. Maggi, C. Adduce, and G. Lane-Serff, "Gravity currents interacting with slopes and overhangs," Adv. Water Resour. **171**, 104339 (2023).
[45]P. Gauer, T. J. Kvalstad, C. F. Forsberg, P. Bryn, and K. Berg, "The last phase of the Storegga slide: Simulation of retrogressive slide dynamics and comparison with slide-scar morphology," Mar. Pet. Geol. **22**, 171–178 (2005).
[46]K. Yam, W. D. McCaffrey, D. B. Ingham, and A. D. Burns, "CFD modelling of selected laboratory turbidity currents," J. Hydraul. Res. **49**, 657–666 (2011).
[47]Z. Xiu, L. Liu, Q. Xie, J. Li, G. Hu, and J. Yang, "Runout prediction and dynamic characteristic analysis of a potential submarine landslide in Liwan 3-1 gas field," Acta Oceanol. Sin. **34**, 116–122 (2015).
[48]Z. Ge, W. Nemec, R. L. Gawthorpe, and E. W. Hansen, "Response of unconfined turbidity current to normal-fault topography," Sedimentology **64**, 932–959 (2017).
[49]Z. Ge, W. Nemec, A. J. Vellinga, and R. L. Gawthorpe, "How is a turbidite actually deposited?," Sci. Adv. **8**, eabl9124 (2022).
[50]R. I. Wilson, H. Friedrich, and C. Stevens, "Turbulent entrainment in sediment-laden flows interacting with an obstacle," Phys. Fluids **29**, 036603 (2017).
[51]D. Liu, Y. Cui, C. E. Choi, N. A. Bazai, Z. Yu, M. Lei, and Y. Yin, "Numerical investigation of deposition mechanism of submarine debris flow," in *Proceedings of the 7th International Conference on Debris-Flow Hazards Mitigation*, June 10–13, Golden, Colorado (2019).
[52]N. Fan, J. Jiang, Y. Dong, L. Guo, and L. Song, "Approach for evaluating instantaneous impact forces during submarine slide-pipeline interaction considering the inertial action," Ocean Eng. **245**, 110466 (2022).
[53]P. A. Allen, R. M. Dorrell, O. Harlen, R. E. Thomas, and W. D. McCaffrey, "Mixing in density-and viscosity-stratified flows," Phys. Fluids **34**, 096605 (2022).
[54]Y. Li, Y. Dong, and G. Chen, "A numerical investigation of transformation rates from debris flows to turbidity currents under shearing mechanisms," Appl. Sci. **13**, 4105 (2023).
[55]H. Cheng, Y. Huang, and Q. Xu, "Numerical modeling of the submarine debris flows run-out using SPH," in *Engineering Geology for Society and Territory* (Springer, 2014), Vol. 4, pp. 157–160.
[56]E. Bertevas, T. Tran-Duc, K. Le-Cao, B. C. Khoo, and N. Phan-Thien, "A smoothed particle hydrodynamics (SPH) formulation of a two-phase mixture model and its application to turbulent sediment transport," Phys. Fluids **31**, 103303 (2019).
[57]Y. Dong, D. Wang, and L. Cui, "Assessment of depth-averaged method in analysing runout of submarine landslide," Landslides **17**, 543–555 (2020).
[58]J.-j. Shi, W. Zhang, B. Wang, C.-y. Li, and B. Pan, "Simulation of a submarine landslide using the coupled material point method," Math. Probl. Eng. **2020**, 4392581.
[59]S. Koshizuka and Y. Oka, "Moving-particle semi-implicit method for fragmentation of incompressible fluid," Nucl. Sci. Eng. **123**, 421–434 (1996).
[60]Y. Huang and C. Zhu, "Numerical analysis of tsunami–structure interaction using a modified MPS method," Nat. Hazards **75**, 2847–2862 (2015).
[61]T. Zhao, G. Houlsby, and S. Utili, "Investigation of submerged debris flows via CFD-DEM coupling," in *Proceedings of the Geomechanics from Micro to Macro IS Cambridge* (Taylor and Francis Group, Cambridge, 2014), pp. 497–502.
[62]J. Xie, P. Hu, C. Zhu, Z. Yu, and T. Pähtz, "Turbidity currents propagating down an inclined slope: Particle auto-suspension," J. Fluid Mech. **954**, A44 (2023).
[63]Y. Lu, X. Liu, J. Sun, X. Xie, D. Li, and X. Guo, "CFD-DEM modeling of turbidity current propagation in channels with two different topographic configurations," Front. Mar. Sci. **10**, 1208739 (2023).
[64]Q. A. Tran, G. Grimstad, and S. A. G. Amiri, "MPMICE: A hybrid MPM-CFD model for simulating coupled problems in porous media. Application to earthquake-induced submarine landslides," arXiv:2211.12761 (2022).
[65]X. Guo, T. Stoesser, D. Zheng, Q. Luo, X. Liu, and T. Nian, "A methodology to predict the run-out distance of submarine landslides," Comput. Geotech. **153**, 105073 (2023).
[66]F. Sahdi, C. Gaudin, J. G. Tom, and F. Tong, "Mechanisms of soil flow during submarine slide-pipe impact," Ocean Eng. **186**, 106079 (2019).
[67]M. Nasr-Azadani and E. Meiburg, "Turbidity currents interacting with three-dimensional seafloor topography," J. Fluid Mech. **745**, 409–443 (2014).
[68]M. I. Cantero, J. R. Lee, S. Balachandar, and M. H. Garcia, "On the front velocity of gravity currents," J. Fluid Mech. **586**, 1–39 (2007).
[69]S. D. An, "Interflow dynamics and three-dimensional modeling of turbid density currents in IMHA reservoir, South Korea," Ph.D. thesis, Colorado State University, 2011.
[70]G. Constantinescu, "LE of shallow mixing interfaces: A review," Environ. Fluid Mech. **14**, 971–996 (2014).
[71]L. Ottolenghi, C. Adduce, R. Inghilesi, V. Armenio, and F. Roman, "Entrainment and mixing in unsteady gravity currents," J. Hydraul. Res. **54**, 541–557 (2016).
[72]J. Pelmard, S. Norris, and H. Friedrich, "Les grid resolution requirements for the modelling of gravity currents," Comput. Fluids **174**, 256–270 (2018).
[73]R. Zhu, Z. He, and E. Meiburg, "Mixing, entrainment and energetics of gravity currents released from two-layer stratified locks," J. Fluid Mech. **960**, A1 (2023).
[74]C. G. Johnson and A. J. Hogg, "Entraining gravity currents," J. Fluid Mech. **731**, 477–508 (2013).
[75]D. Han, Y. Guo, P. Jiao, Y. Yuan, Y.-T. Lin, and Z. He, "Coherent structures, turbulence intermittency, and anisotropy of gravity currents propagating on a rough and porous bed," Phys. Fluids **35**, 016611 (2023).
[76]A. Zakeri, K. Høeg, and F. Nadim, "Submarine debris flow impact on pipelines—Part II: Numerical analysis," Coastal Eng. **56**, 1–10 (2009).
[77]Y. Zhang, Z. Wang, Q. Yang, and H. Wang, "Numerical analysis of the impact forces exerted by submarine landslides on pipelines," Appl. Ocean Res. **92**, 101936 (2019).
[78]X. Qian, J. Xu, Y. Bai, and H. S. Das, "Formation and estimation of peak impact force on suspended pipelines due to submarine debris flow," Ocean Eng. **195**, 106695 (2020).
[79]X. Guo, X. Liu, M. Li, and Y. Lu, "Lateral force on buried pipelines caused by seabed slides using a CFD method with a shear interface weakening model," Ocean Eng. **280**, 114663 (2023).
[80]R. J. Lowe, J. W. Rottman, and P. Linden, "The non-Boussinesq lock-exchange problem. Part 1. Theory and experiments," J. Fluid Mech. **537**, 101–124 (2005).
[81]Y. Liu, T. Stoesser, and H. Fang, "Effect of secondary currents on the flow and turbulence in partially-filled pipes," J. Fluid Mech. **938**, A16 (2022).
[82]Y. Liu, T. Stoesser, and H. Fang, "Impact of turbulence and secondary flow on the water surface in partially filled pipes," Phys. Fluids **34**, 035123 (2022).
[83]P. Ouro, B. Fraga, N. Viti, A. Angeloudis, T. Stoesser, and C. Gualtieri, "Instantaneous transport of a passive scalar in a turbulent separated flow," Environ. Fluid Mech. **18**, 487–513 (2018).
[84]J. Bai, H. Fang, and T. Stoesser, "Transport and deposition of fine sediment in open channels with different aspect ratios," Earth Surf. Processes Landforms **38**, 591–600 (2013).
[85]B. Chen, B. Fraga, and H. Hemida, "Large-eddy simulation of enhanced mixing with buoyant plumes," Chem. Eng. Res. Des. **177**, 394–405 (2022).
[86]F. Nicoud and F. Ducros, "Subgrid-scale stress modelling based on the square of the velocity gradient tensor," Flow, Turbul. Combust. **62**, 183–200 (1999).
[87]A. J. Chorin, "Numerical solution of the Navier-Stokes equations," Math. Comput. **22**, 745–762 (1968).
[88]M. Cevheri, R. McSherry, and T. Stoesser, "A local mesh refinement approach for large-eddy simulations of turbulent flows," Int. J. Numer. Methods Fluids **82**, 261–285 (2016).
[89]P. Ouro, B. Fraga, U. Lopez-Novoa, and T. Stoesser, "Scalability of an Eulerian-Lagrangian large-eddy simulation solver with hybrid MPI/OpenMP parallelisation," Comput. Fluids **179**, 123–136 (2019).
[90]R. McSherry, K. Chua, T. Stoesser, and S. Mulahasan, "Free surface flow over square bars at intermediate relative submergence," J. Hydraul. Res. **56**, 825–843 (2018).

[91]Q. Luo, G. Dolcetti, T. Stoesser, and S. Tait, "Water surface response to turbulent flow over a backward-facing step," J. Fluid Mech. **966**, A18 (2023).
[92]P. Ouro and T. Stoesser, "Impact of environmental turbulence on the performance and loadings of a tidal stream turbine," Flow, Turbul. Combust. **102**, 613–639 (2019).
[93]K. V. Chua, B. Fraga, T. Stoesser, S. Ho Hong, and T. Sturm, "Effect of bridge abutment length on turbulence structure and flow through the opening," J. Hydraul. Eng. **145**, 04019024 (2019).
[94]C. Gualtieri, A. Angeloudis, F. Bombardelli, S. Jha, and T. Stoesser, "On the values for the turbulent Schmidt number in environmental flows," Fluids **2**, 17 (2017).
[95]V. Dyakova and D. Polezhaev, "Shear instability at the interface between fluid and granular medium in a horizontal rotating cylinder," Phys. Fluids **35**, 043336 (2023).
[96]D. Mohrig, C. Ellis, G. Parker, K. X. Whipple, and M. Hondzo, "Hydroplaning of subaqueous debris flows," Geol. Soc. Am. Bull. **110**, 387–394 (1998).
[97]T. Ilstad, J. G. Marr, A. Elverhøi, and C. B. Harbitz, "Laboratory studies of subaqueous debris flows by measurements of pore-fluid pressure and total stress," Mar. Geol. **213**, 403–414 (2004).
[98]N. Fan, T.-k. Nian, H.-b. Jiao, X.-s. Guo, and D.-f. Zheng, "Evaluation of the mass transfer flux at interfaces between submarine sliding soils and ambient water," Ocean Eng. **216**, 108069 (2020).
[99]F. De Blasio, A. Elverhøi, D. Issler, C. Harbitz, P. Bryn, and R. Lien, "Flow models of natural debris flows originating from overconsolidated clay materials," Mar. Geol. **213**, 439–455 (2004).
[100]Q. Zhang, S. Draper, L. Cheng, M. Zhao, and H. An, "Experimental study of local scour beneath two tandem pipelines in steady current," Coastal Eng. J. **59**, 1750002 (2017).
[101]C. Von Hirschhausen, C. Gerbaulet, C. Kemfert, C. Lorenz, and P.-Y. Oei, *Energiewende "Made in Germany": Low Carbon Electricity Sector Reform in the European Context* (Springer, 2018).
[102]Y. Li, M. C. Ong, D. R. Fuhrman, and B. E. Larsen, "Numerical investigation of wave-plus-current induced scour beneath two submarine pipelines in tandem," Coastal Eng. **156**, 103619 (2020).
[103]F. Zhang, Z. Zang, M. Zhao, J. Zhang, B. Xie, and X. Zou, "Numerical investigations on scour and flow around two crossing pipelines on a sandy seabed," J. Mar. Sci. Eng. **10**, 2019 (2022).
[104]M. Huang, J. Xu, Z. Luan, M. Liu, X. Li, and B. Liu, "Analysis of DF1-1 subsea pipeline free-span distribution characteristics and rectification effects," Mar. Sci. **45**, 77–87 (2021).
[105]X.-s. Guo, D.-f. Zheng, L. Zhao, C.-w. Fu, and T.-k. Nian, "Quantitative composition of drag forces on suspended pipelines from submarine landslides," J. Waterw., Port, Coastal, Ocean Eng. **148**, 04021050 (2022).